Contents

11. A Simulation Model of Time-Dependent Plasma-Spacecraft Interactions

P.L. Rothwell, A.G. Rubin, and G.K. Yates
Air Force Geophysics Laboratory
Hanscom AFB, Mass.

Abstract

A plasma simulation code is presented that models the time-dependent plasma properties in the vicinity of a spherical, charged spacecraft. After showing agreement with analytic, steady-state theories and ATS-6 satellite data, the following three problems are treated: (1) transient pulses from photoemission at various emission temperatures and ambient plasma conditions, (2) spacecharge limited emission, [1] and (3) simulated plasma oscillations in the long-wavelength limit ($k\lambda_D << 1$).

1. INTRODUCTION

1.1 Model Objectives

The objective of this computer model is to realistically simulate plasma-spacecraft interactions. It presently treats time-dependent plasma phenomena in the limit of spherical symmetry. Although future plans anticipate the incorporation of a realistic three-dimensional spacecraft geometry, understanding of the spherically symmetric limit uniquely identifies plasma effects. In this manner, it is

hoped that the model will prove to be a useful tool in differentiating between plasma and geometric phenomena observed in the SCATHA satellite data.

1.2 Description of the Model

We use what is commonly called a "particle pusher" model. That is, one approximates the actual plasma by a number of "computer" particles whose charge, position, angular momentum, and velocity are tracked in time. By properly weighting these computer particles, reasonable statistics can be obtained near the spacecraft. [2]

Appropriate particle distributions are generated either by a Monte Carlo technique or by a systematic loading of the velocity and spatial intervals ("quiet start"). [3]

For purposes of comparison, we have initially restricted ourselves to Maxwellian distributions. However, both methods (Monte Carlo and Quiet Start) can easily be extended to any distribution that can be numerically integrated. Once the neutral plasma is created, the computer tracks the particles and recalculates the potential at each time step. Particles that hit or are emitted from the spacecraft are taken into account as well as those that enter and exit the sheath boundary. Thus, the computerized sheath structure dynamically evolves in analogy with the physical situation. One may then store the results and restart the program with a new set of environmental parameters.

In Section 2 of this paper, we will show the agreement of the present work with that of other approaches and with the ATS-6 data. Section 3 deals with the photosheath. The minimum rise time of the spacecraft potential is determined for various emission temperatures and ambient plasma parameters. Space charge effects are also discussed as well as those due to secondary emission and backscattering. Finally, in Section 4, we illustrate the possible presence of plasma oscillations by performing "computer experiments" with the code.

2. COMPARISON WITH ANALYTIC APPROACHES

2.1 Comparison with Langmuir Theory

As a first step we compared our steady-state results with those expected from Langmuir theory. [4, 5] Figure 1 shows the comparison. In these results, the ambient plasma temperature and density were held fixed and the fixed potential on the probe (spacecraft) increased. The parameter I_p is the ambient current to the probe surface at zero voltage. If one makes the same assumption for the model as for the Langmuir theory (that is, no presheath acceleration), good agreement is

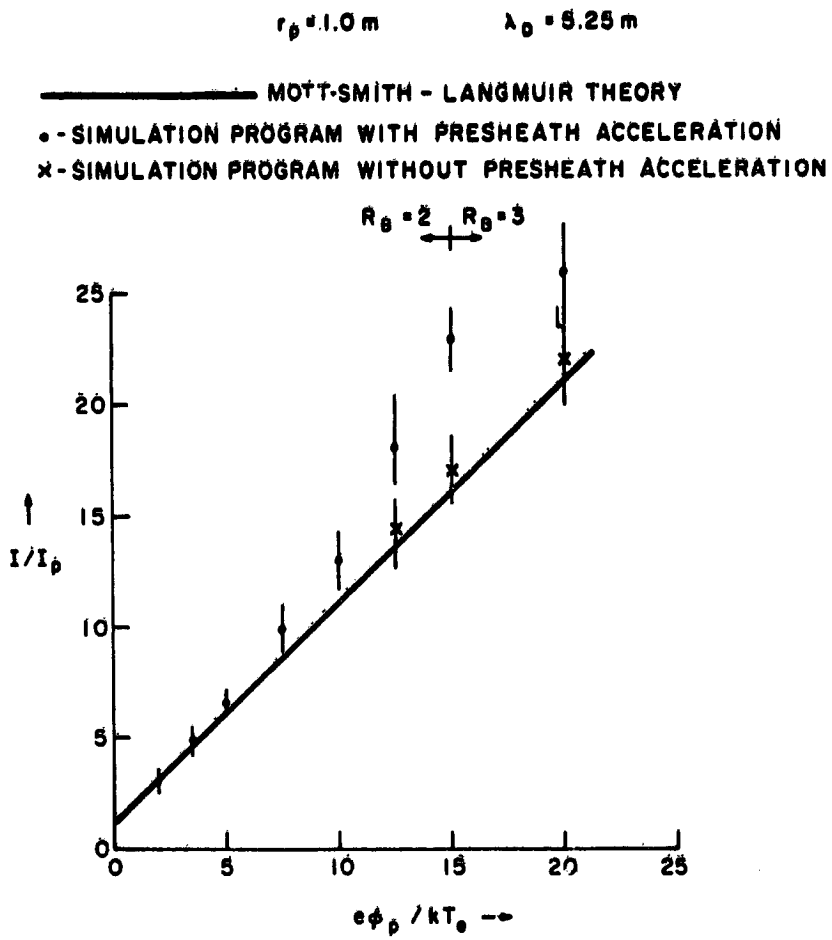

Figure 1. Comparison of the Simulation Code with the Mott-Smith-Langmuir Theory. This figure depicts a current-voltage curve in the thick-sheath approximation. The probe radius is 1 m and the outer sheath boundary has been set to R_B = 2 and R_B = 3 in units of λ_D. The dots represent the case where there is presheath acceleration. That is, when the potential at R_B is nonzero

obtained. (Presheath acceleration takes into account the dependence of the sheath size on the probe potential. In the code, this is represented by a Boltzmann factor at the sheath boundary.[2])

2.2 Comparison with Static Codes

We also compared our results in the steady-state limit to numerical solutions of the Vlasov and Poisson equations.[6,7] The steady-state limit is reached by allowing an initially neutral plasma to form a sheath around a voltage-biased probe. Figure 2 shows the code results after 0.17 msec. In this example, the probe has a bias voltage equal to minus ten times the average electron energy expressed in electron volts. From Figure 2 it is seen that both methods give the same voltage profile, but differ somewhat for the electron density at large r. This difference is probably due to the time-dependent code not having reached the true steady-state values.

Figure 3 shows a similar comparison for relatively intense monoenergetic electron emission from the probe surface.[8] The probe is positively biased at +2.0 volts. The emission energy is +1.0 electron volts so that all emitted electrons return to the probe surface. The resultant density and voltage profiles show good agreement. Scatter in the time-simulation results can be improved by using more computer particles. For example, in the present case we used approximately 4000 computer ions and electrons. This number can be significantly increased at the expense of longer computation time.

2.3 Comparison with ATS-6 Data

Two charging events in the eclipse region were analyzed from ATS-6 data supplied by DeForest.[9] The proton and electron temperature during these events as well as the simultaneous vehicle potential are shown in Table 1.[10] These two events represent a time when injection of hot plasma took place. Also shown in Table 1 are the vehicle potentials as predicted from a simple Boltzmann approximation and a thick-sheath approximation to the orbit-limited Langmuir theory.

The Boltzmann approximation assumes that the electron density is closely represented by $N_e = N_{eo} e^{-e\phi_p/kT_e}$. Protons are considered to be unaffected. Therefore, current balance is given by

$$\epsilon \left(\frac{kT_e}{m_e}\right)^{1/2} e^{-|e\phi_p|/kT_e} = \left(\frac{kT_p}{m_p}\right)^{1/2} \tag{1}$$

or

$$e\phi_p/kT_e = \ell n \left[\epsilon t_e m_p / t_p m_e\right]^{1/2}$$

where m_p = proton mass, m_e = electron mass, k = Boltzmann constant and ϵ is defined below.

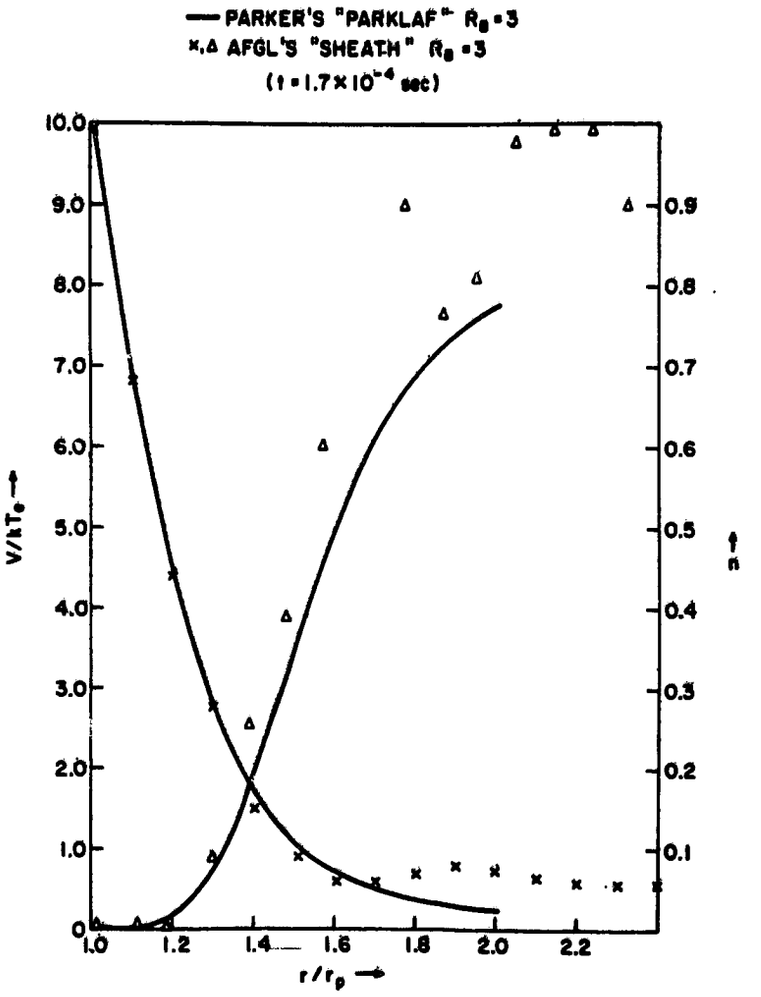

Figure 2. Potential and Density Profiles in the Sheath. Comparison of the time-dependent code with a steady-state numerical solution to the Vlasov-Poisson equations (L. W. Parker, private communication). The density, n, is normalized to its ambient value. The potential, V, is shown normalized to the electron temperature. The parameter, t , is the time at which the time-dependent results were taken. A negative bias of -10 kT_e volts is on the spacecraft surface. R_B is expressed in units of probe radii

R_0 = 1m
EMISSION CURRENT = 10^{-5} amp/m^2
EMISSION ENERGY = 1eV (monoenergetic electrons)
EMISSION DENSITY = 211/cm^3
AMBIENT TEMPERATURE = 5eV (Maxwellian)
AMBIENT DENSITY = 1/cm^3
Φ_0 = +2V = Sphere Potential (quasi-equilibrium) vs. +1V equilibrium

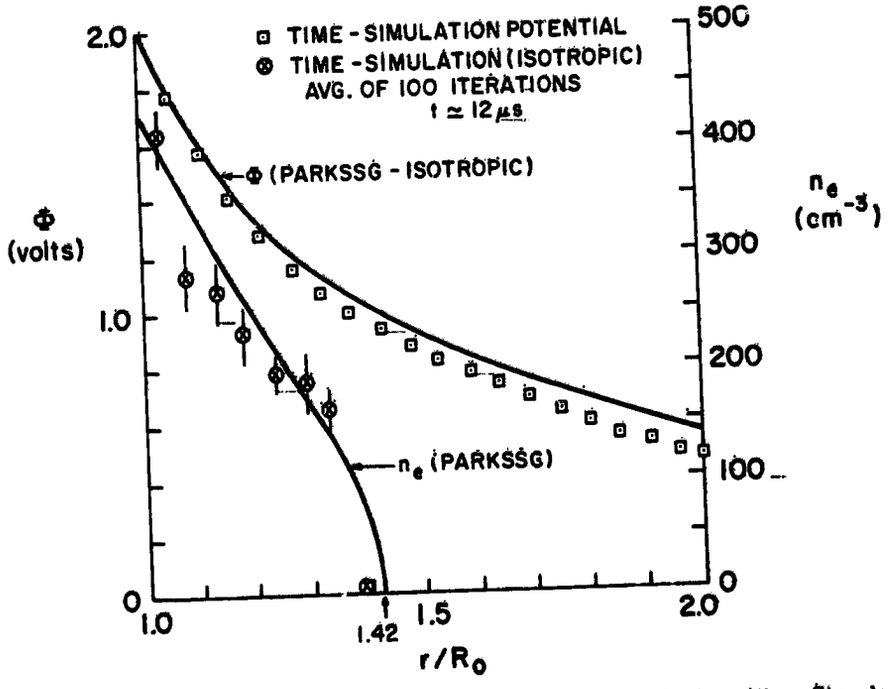

Figure 3. Comparison of the Time-Dependent Code with a Steady-State Numerical Solution with Monoenergetic Emission. R_0 = satellite radius. PARKSSG is a code developed by L. W. Parker that includes electron surface emission. See reference 8

Table 1. Comparison of Boltzmann and Langmuir Theories with ATS-6 Data. ϵ = 0.16

Day of Event (1976)	T_p	T_e	$\lvert e\phi\rvert/kT_e$		
			Meas.	Boltzmann	Langmuir Thick-Sheath
59	23.7	9.1	1.15	1.45	1.10
66	73.2	8.8	0.79	0.86	0.78

The Langmuir thick-sheath approximation is more realistic in that it also takes into account the effect of the spacecraft potential on the net proton current. It is given by

$$\epsilon\left(\frac{kT_e}{m_e}\right)^{1/2} e^{-|e\phi_p|/kT_e} = \left(\frac{kT_p}{m_p}\right)^{1/2} (1 + e\phi_p/kT_p) \qquad (2)$$

a transcendental equation in the satellite potential, ϕ_p, which can be reduced to a quadratic equation in $(T_e/T_p)^{1/2}$. The parameter, ϵ, represents the net fractional electron current to the spacecraft and, thus, takes into account secondary emission, backscattering and photoemission. In Table 1 we have set $\epsilon = 0.16$ (that is, 84 percent net backscatter, etc.) for both approximations. Examination of Eq. (2) shows that in the limit of large proton temperatures the thick-sheath approximation reduces to the Boltzmann case. This is also seen from Table 1. In both cases, the Langmuir thick-sheath approximation gives better agreement with measured results than the Boltzmann limit.

Insight into the expected sensitivity of spacecraft voltage to changes in the ambient current, can be seen from Figure 4 which contains a plot of Eq. (2). The top-half of this figure is a linear scale plot of normalized voltage to the net electron current incident on the spacecraft normalized to the ambient electron current (with the Boltzmann factor). The bottom half of the figure shows the same curve on a log-log scale plot. These curves will be modified by any voltage dependence in ϵ such as space charge limiting effects.

In conclusion, for large negative spacecraft potentials, the thick-sheath approximation predicts the average spacecraft voltage, given the proper material characteristics and the ambient electron and proton temperatures. The code is consistent with the thick-sheath limit, and predicts sheath density and voltage profiles. The simulation code, however, is also valid where the thick-sheath approximation breaks down. That is, where space charge and time-dependent effects become important.

The importance of space charge is determined by comparing the spacecraft surface charge to the charge residing in the sheath. For large surface potentials and continuous plasmas, spacecraft surface charge is dominant. In that case, Laplacian solutions with appropriate geometric boundary conditions should be adequate. At low vehicle potentials with surface emission, space charge effects become important.

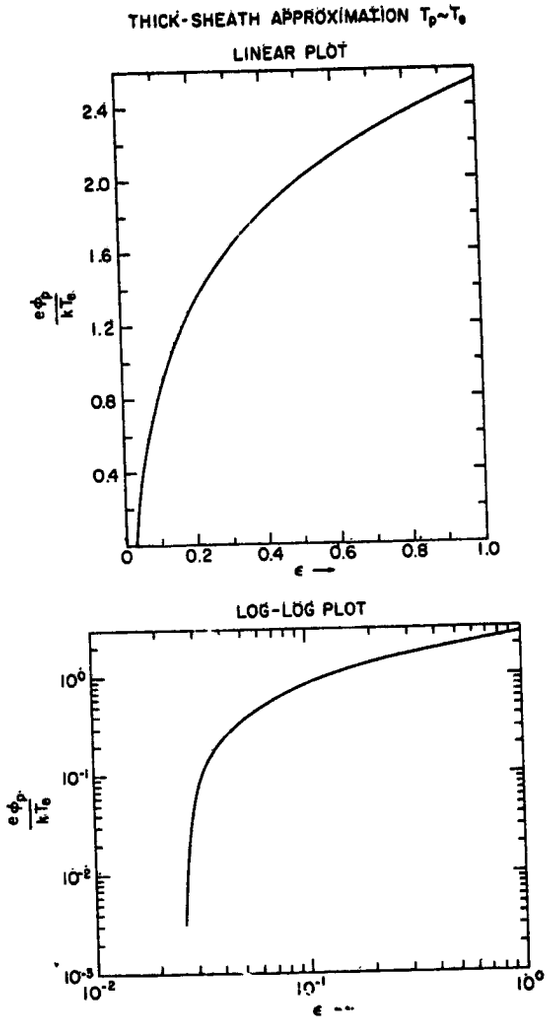

Figure 4. Spacecraft Voltage versus Net Electron Current as Normalized to the Ambient Current (Including the Boltzmann Factor)

3. THE PHOTOSHEATH

3.1 Introduction

Incident sunlight causes the emission of low energy (~2 eV) electrons from the satellite surface. This emission, in a hot plasma environment, sometimes swings the satellite potential thousands of volts as the satellite enters and emerges

from the eclipse region. A second effect of photoemission is its background effect on ambient plasma density measurements. These measurements must be corrected for electrons originating on the satellite surface. A third effect of the photosheath is its possible interaction with onboard electron emitters either through space-charge limiting effects or by stimulation of plasma oscillations.

In the present code, we can simulate either monoenergetic or Maxwellian photoemission. The Maxwellian case is described in detail in Appendix A. The angular distribution of the emitted photoelectrons follow a cosine law relative to the surface normal.[11] In the following paragraphs, we consider photoemission to be switched "on" at t = 0. This is a worst case condition since satellites emerge from eclipse over a period of minutes.

3.2 Monoenergetic Emission

Figure 5 shows the simulation results for monoenergetic emission. The vertical axis represents the satellite (taken as a 1 m radius sphere) potential while the horizontal axis denotes time in microseconds. The satellite is taken to be at zero volts at t = 0. The bump in each of the curves occurs when the initially emitted electrons return to the satellite. The final surface is the result of two effects. First, emitted electrons do not return until the satellite reaches a voltage

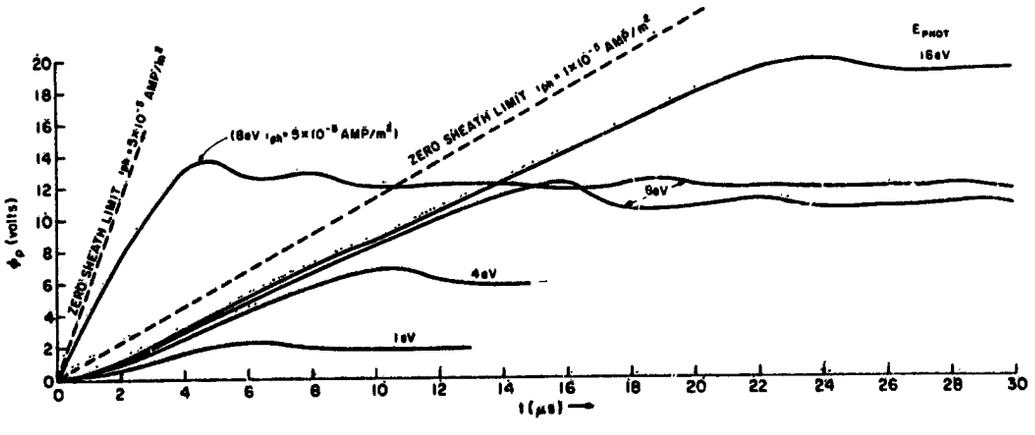

Figure 5. Monoenergetic Emission in a Tenuous Plasma. The emission is assumed to be switched "on" at t = 0. This represents a worst case condition. The abscissa is in microseconds

equal to the emission energy. Secondly, there is a finite transit time for the returning electrons. This means that the final voltage is higher than the emission energy expressed in electron volts. The dotted lines represent spacecraft voltage buildup in the limit where all emitted electrons escape. Further cases regarding monoenergetic photoemission can be found in Katz et al. [12]

3.3 Transient Rise-Time

Figure 6 shows expected surface voltage rise-times at various ambient densities. In these runs the photoelectrons are emitted with a Maxwellian distribution with a temperature corresponding to 6 eV. [13] The ambient density is then varied to determine the rise-time sensitivity to the ratio of the photoelectron and ambient currents.

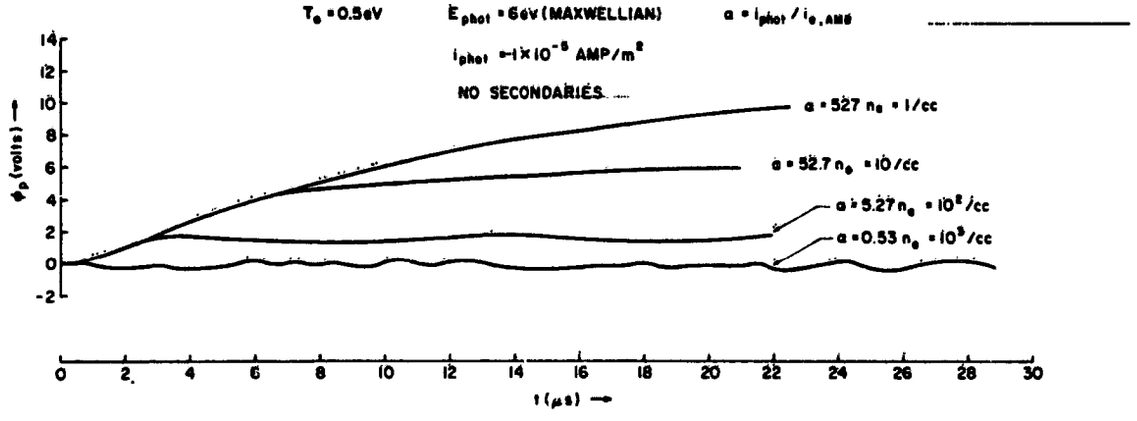

Figure 6. Spacecraft Voltage Transients for a Fixed Emission Temperature and Various Plasma Densities. No secondaries included

In Figure 7, we treat the alternative case. That is, the ambient plasma parameters are held constant and the photoemission temperature is varied. The dotted line represents 100 percent escape efficiency for the emitted electrons. The steady-state surface voltage, as expected is dependent on emission temperature.

The transients shown in Figures 6 and 7 could cause satellite malfunctions if they reached a critical logic circuit. Integrated circuits usually operate over 0-5 volts so that a $\gtrsim$ 2 volt transient through the ground lines would give a false

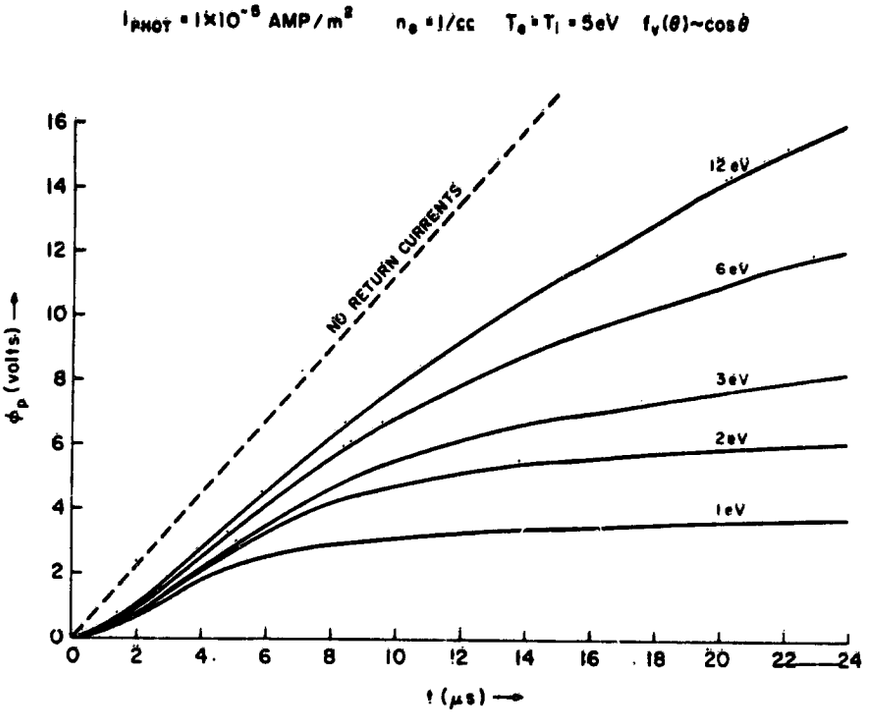

Figure 7. Transient Spacecraft Potentials for Strong Photoemission at Various Emission Temperatures. No secondaries included

signal. The incident sunlight flux must change more rapidly than the characteristic time-constant of the surface materials. Otherwise, these rise times will not be significant. Further research into this area needs to be performed.

3.1 Space Charge Limited Emission

Chang and Bienkowski[14] showed that large current emission from a positively biased probe is inhibited by space-charge buildup in front of the surface. (See center Figure 8.) Whipple[1] used a similar approach to show that differential surface charging is necessary to explain the barrier potentials observed on ATS-6. In this section, we use the simulation code to produce space-charge effects. Application is then made to a floating spacecraft potential with and without active control experiments.

The versatility of the present code is illustrated in the lefthand side of Figure 8. The surface potential is held fixed at +6 volts while the electronemission current is increased. For a nominal 5×10^{-5} A/m^2 photoemission current density, no

CHANG AND BIENKOWSKI
(PHYS. OF FLUID, VOL.13, 902, 1970)

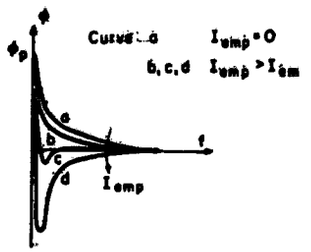

TYPICAL POTENTIAL DISTRIBUTIONS OF A POSITIVELY BIASED PROBE IN THE PRESENCE OF ELECTRON EMISSION.

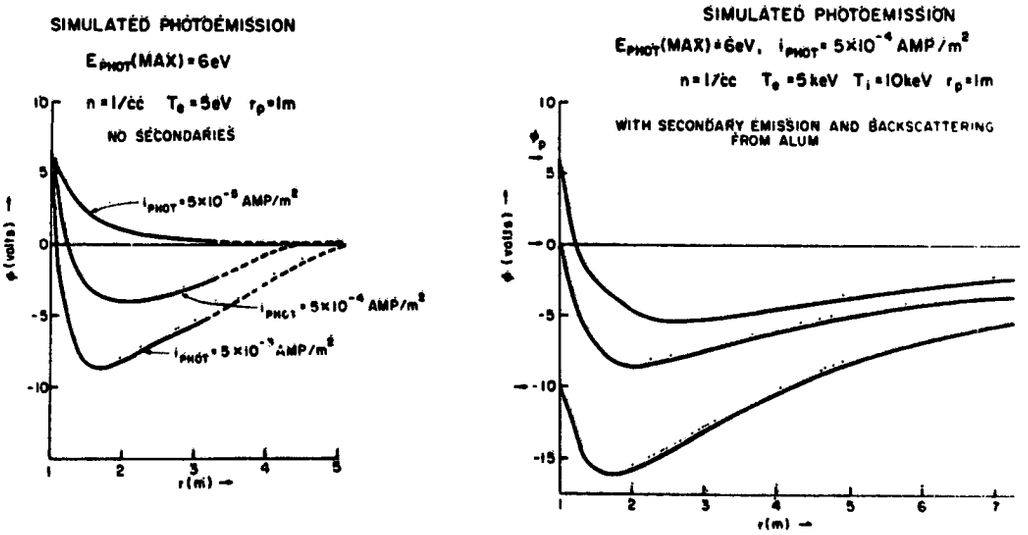

Figure 8. Simulated Maxwellian Emission Showing Potential Barriers. The lefthand figure shows the barrier depth as a function of emission intensity. (The higher values of i_{phot} are, of course, unrealistic and are used solely to illustrate the barrier). The righthand figure shows the barrier as a function of surface potential

potential barrier is observed. However, if the emission is artificially enhanced to 50 and 500×10^{-5} A/m^2 potential barriers are clearly evident and inhibit further emission. (In these runs, the sheath boundary was chosen at 3.32 m). The effect of the potential barrier is such that only 57.3 percent, 22.2 percent and 4.4 percent of the emitted flux reaches 3.32 m for the three respective cases. These results show that the simulation code can treat space-charge effects and predict emission efficiencies. The code can distinguish between emitted and ambient particles and, therefore, can be used to correct ambient plasma measurements.

The depth of the potential well is also dependent on the satellite voltage. On the righthand side of Figure 8 we show three curves for the same ambient and emission characteristics but at different surface potentials. For large negative values of the surface potential, the well is completely eliminated since emitted electrons are rapidly repelled. On the other hand, if the surface potential is too positive, the emitted electrons quickly return to the emitting surface and a significant spacecharge cannot form. Therefore, potential wells are expected for only a specific range of surface potentials.

The situation is more complex with a floating spacecraft potential. In this case, both the well depth and the surface voltage are strongly dependent on the net electron current. Figure 9 shows the expected voltage profile in the sheath at various emission currents and ambient densities. Runs were taken at three densities n = 1 cm^{-3}, 5 cm^{-3} and 10 cm^{-3} with a photoemission current of 8.2 μ A/m^2.[15] The emitted current was then increased to 40 μ A/m^2 which is the limiting photoemission intensity for aluminum.[16] In addition to photoemission, 84 percent of the incident electrons were assumed to cause isotropic secondaries to be emitted with a Maxwellian energy distribution (kT = 2.5 eV). The 84 percent figure was estimated from ATS-6 eclipse data (Table 1). Figure 9 shows that the presence of a potential well is dependent on a "balance" between the ambient and emitted currents. Space charge also gives rise to the curious effect that a spacecraft may have a net positive charge but be at a negative potential relative to the ambient plasma.

The Figure 9 also shows the maximum barrier to be about -3 volts. These results are in agreement with those of Whipple[1] who showed that the barrier potentials inferred from ATS-6 data are too large to be explained in terms of a spherically symmetric photoelectron or secondary sheath surrounding a uniformly charged spacecraft. Differential charging between spacecraft surfaces is, therefore, mainly responsible for the potential barrier. The average satellite potential relative to the ambient plasma, however, is determined by the sheath.

Active control experiments in hot dense plasma could lead to more pronounced space-charge effects. As an extreme example, we took T_e = 9.1 k eV, T_i = 23.7 k eV and n = 5×10^4 cm^3. In that case in order to maintain neutrality, electron emission

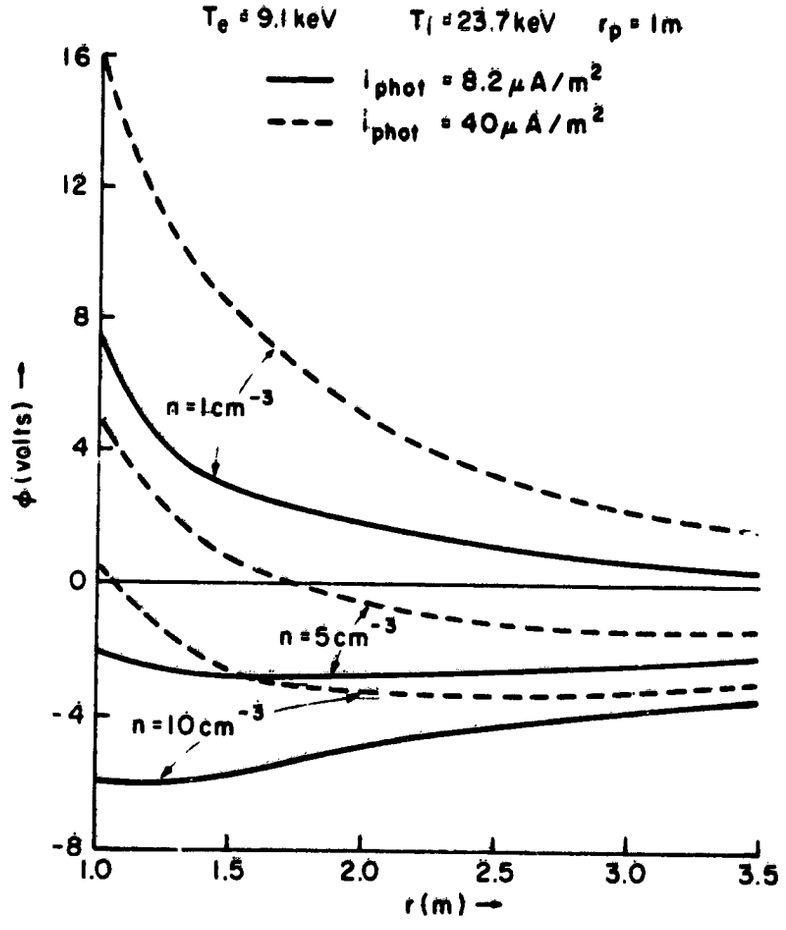

Figure 9. The Potential Profile in the Sheath at Various Emission Intensities and Ambient Densities. The surface potential is floating

of ~1.6 A was required. A potential barrier on the order of hundreds of volts was obtained.

3.5 Future Plans

The Monte-Carlo approach is presently being applied to include realistic backscattering and secondary emission from both electrons and incident ions. These processes are energy and material dependent. In this way, insight into the importance of material properties on spacecraft charging will be gained.

4. PLASMA OSCILLATIONS

4.1 Introduction

Because of the dynamic nature of the plasma, the sheath potential may oscillate in time. Moving plasma particles "overshoot" their equilibrium positions and undergo simple harmonic motion. Collective oscillations are, therefore, closely connected with dynamic screening.[17] The natural frequency of these collective modes is the plasma frequency,

$$\omega_{P_e} = \left(\frac{4\pi e^2 n}{m_e}\right)^{1/2}$$

where n is the ambient plasma density. The sheath, therefore, is like a resonant cavity that oscillates under certain perturbations.

4.2 Observation of Plasma Oscillations

Initially, we looked for plasma oscillations in the thin-sheath limit. An ambient density of 200 cm^{-3} and an electron-ion temperature $T_e = T_i = 0.2$ eV was chosen. This gives a Debye length of 0.235 m compared with a 1 m probe radius. The probe potential was biased at +1.0 volt. The top three curves in Figure 10 show the sheath potential profile at 10 μsec intervals. Some time-dependence is observed but its coherent property is not clear. The periodic nature of the time-dependence is enhanced by plotting the potential at a constant distance (r = 2.60 m) from the probe surface as shown in the bottom part of Figure 10. The local potential oscillates at a frequency comparable with the plasma frequency ($\omega_{pe} = 7.99 \times 10^5$ rad/sec). The nature of this oscillation is further delineated by performing a computer experiment.

4.3 A Computer Experiment

Figure 11 represents a computer experiment in which all the parameters except the ambient density remained constant. The ambient density in each curve is higher by a factor of 2 compared with the curve immediately above it. The points represent 10 iteration averages and the error bars the rms deviation from this average. The observation point was taken at approximately 16 λ_D (λ_D = Debye length) in each run. The average and standard deviation of the oscillation period, as estimated from these plots, is also given. In each instance the observed averaged period, T, is shorter than the plasma period $\tau = 1.11 \times 10^{-4}/\sqrt{n}$ sec). In order to estimate the oscillation wavelength, λ, the one-dimensional plasma

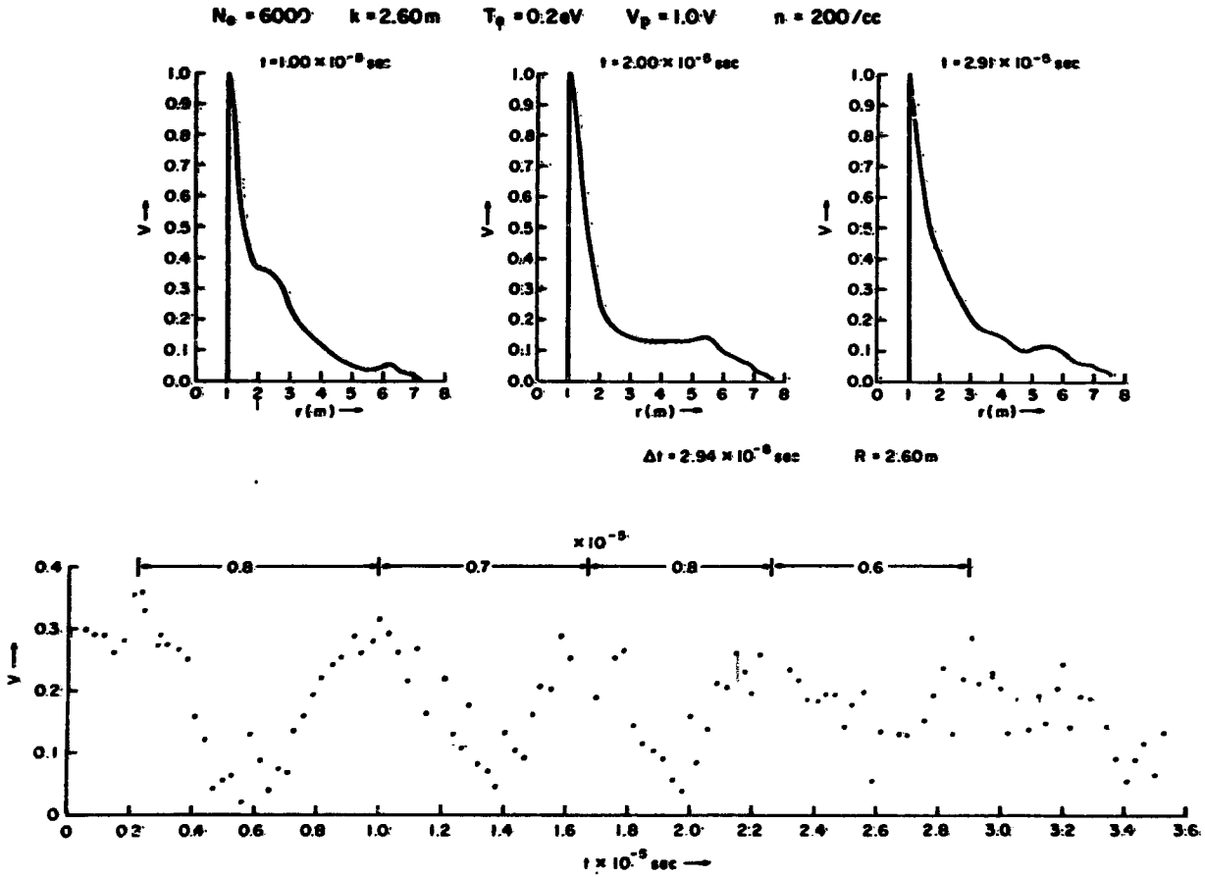

Figure 10. The Top Three Figures Denote the Sheath Potential Profile at 10 μsec intervals. The time-step for each iteration was 29.4 ns. The bottom curve is a time-history of the voltage at a fixed position. Time is measured in units of 10^{-5} sec

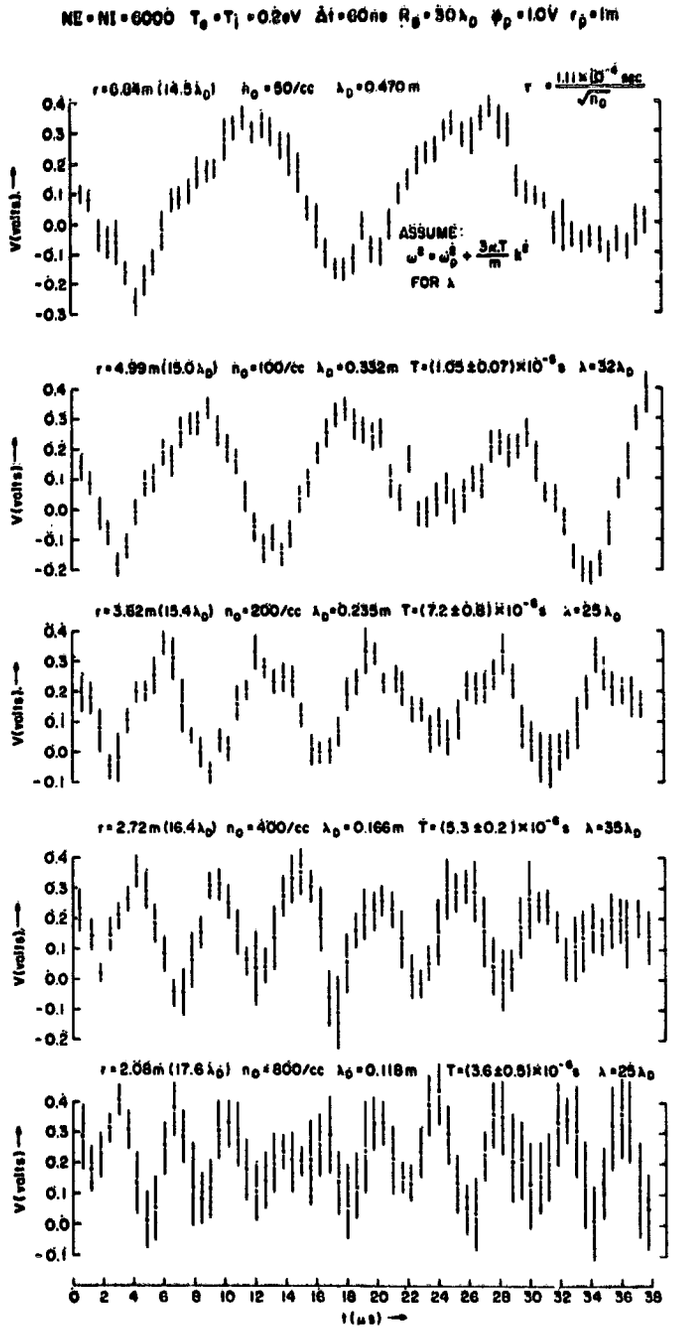

Figure 11. Simulated Plasma Oscillations. Each curve represents the voltage time-history for various densities. NE and NI are the number of computer electrons and ions respectively. Time is in microseconds. λ denotes wavelength which equals $2\pi/k$

dispersion relation[17] is used. Although this is derived for a cartesian geometry, we assume it also holds for the spherical case in the thin sheath limit. The relation is

$$\omega^2 = \omega_{P_e}^2 + 3 \langle kT \rangle k^2/m \tag{3}$$

where

λ = $2\pi/k$, ω = observed frequency, ω_{pe} = plasma frequency

$\langle kT \rangle$ = mean electron energy

m = electron mass

k = wavenumber .

The respective wavelengths, as obtained from Eq. (3), are shown on the righthand side of Figure 11. The central values of T were used. Results imply a wavelength on the order of the sheath thickness ($R_B - r_p$). Since the surface voltage is fixed at +1.0 volt and is close to zero at R_B, the analogy between the sheath and a resonant cavity is seen to be very close.

Plasma oscillations are Landau-damped by the transfer of wave energy to electrons traveling slightly below the wave phase velocity, $V_p = \omega/k$. To test the present code we artificially enhanced the high energy tail of the Maxwellian electron distribution but retained the condition $\partial f/\partial V < 0$. Under these conditions the wave amplitude shown in Figure 11 significantly decreased indicating, as expected, enhanced damping.

The oscillations shown in Figure 11 approach the long wavelength limit, $k\lambda_D < 1$. In that case, there is an analytic expression[17] for the rate of damping. It is

$$\gamma = \sqrt{\frac{\pi}{8}} \frac{\omega_{P_e}}{(k\lambda_D)^3} \text{ EXP } \left(-\frac{3}{2} - \frac{1}{2k^2\lambda_D^2} \right) \tag{4}$$

where γ = decay rate (sec^{-1}), ω_{P_e} = electron plasma frequency. While there is substantial fluctuation in γ from its sensitivity to k, the shortest decay time is 190 μsec for $\bar{n}$ = 800 cm^{-3} run. This is sufficiently long so that no significant damping is expected to be seen in Figure 11.

At long wavelengths the wave phase velocity, V_p, is much greater than the thermal electron velocity so that there are few electrons in the resonant region. At shorter wavelengths ($k\lambda_D \sim 1$) the wave phase velocity approaches the thermal particle velocity. The presence of many electrons in this velocity region rapidly damps the plasma wave. While the above results imply the usefulness of plasma simulation techniques in looking at collective behavior, some caution should be noted.

The basic problem is that the observed oscillations can be either physically stimulated or artifically driven by high frequency grid or computer "noise" that couples to the lower frequency plasma oscillation by aliasing.[18] The computer code should be sufficiently free from noise so that observed oscillations are consistent with analytic criteria.[3] The most common technique for reducing noise is to treat the computer particles as having a finite size[19] and to periodically smooth the distribution function in both velocity and spatial coordinates.[20] These sophistications should delineate the origin and nature of the oscillations.

5. SUMMARY AND CONCLUSIONS

Agreement has been shown between a time-dependent simulation code and steady-state solutions to the Vlasov-Poisson equations. Transient voltage rise-times due to photoemission were presented and space-charge limiting effects discussed. Finally, a computer "experiment" was presented that showed the presence of plasma waves. Caution is noted for possible aliasing effects.

It is concluded, based on the above results, that a simulation approach is a valuable and versatile method for dealing with complex, plasma-related space phenomena. In particular, additional features can be added as building blocks with little modification of the existing code. Care should be taken, however, in distinguishing between computer-related and physically-related effects.

Acknowledgments

We would like to thank Lee W. Parker for many interesting conversations on the probe problem and C. P. Pike for his helpful comments. Finally, we would like to thank Mary Spanos and Louise Peterson for their assistance in preparing the manuscript.

References

1. Whipple, E. C., Jr. (1976) Theory of the spherically symmetric photoelectron sheath: A thick sheath approximation and comparison with ATS-6 observation of a potential barrier, J. Geophys. Res. 81:601-607.

2. Rothwell, P. L., Rubin, A. G., Pavel, A. L., and Katz, L. (1976) Simulation of the plasma sheath surrounding a charged spacecraft in Spacecraft Charging by Magnetospheric Plasmas, A. Rosen, Editor, M. I. T. Press, Cambridge, MA and London, England.

3. Matsuda, Y., and Crawford, F. W. (1975) Computational study of nonlinear plasma waves: 1. Simulation model and monochromatic wave propagation, Phys. Fluids 18:1336-1353.

4. Chen, F. F. (1965) Electric probes, in Plasma Diagnostic Techniques by R. H. Huddlestone and S. L. Leonard, Editors, Academic Press, New York.

5. Laframboise, J. G. (1966) Theory of Spherical and Cylindrical Langmuir Probes in a Collisionless, Maxwellian Plasma at Rest, Univ. of Toronto Rpt. 100, Toronto, Canada.

6. Parker, L. W., and Whipple, E. C. Jr., (1970) Theory of spacecraft sheath structure, potential and velocity effects on ion measurements by traps and mass spectrometers, J. Geophys. Res. 75:4720-4733.

7. Parker, L. W., and Whipple, E. C. Jr., (1967) Theory of a satellite electrostatic probe, Ann. Phys. 44:126-161.

8. Parker, L. W. (1976) Theory of Electron Emission Effects in Symmetric Probe and Spacecraft Sheaths, AFGL-TR-76-0294.

9. DeForest, S. E. (1976) Private Communications.

10. Garrett, H. B. (1977) Analysis of Penumbral Eclipse Data, this volume.

11. Fadley, C. S. (1973) Theoretical aspects of x-ray photoelectron spectroscopy, Electron Emission Spectroscopy, Dekeyser, W., Fiermans, L., Valderkelen, G., and Vernik, J., D. Reidel Publishing Co., Dordrecht-Holland, pp. 151-224.

12. Katz, I., Wilson, A., Parker, L. W., Rothwell, P. L., and Rubin, A. G. (1976) Static and dynamic behavior of spherical probe and satellite plasma sheaths, IEEE Annual Conf. on Nuclear & Space Radiations Effects, San Diego, CA, July.

13. Wrenn, G. L., and Heikkila, W. J. (1973) Photoelectrons emitted from Isis spacecraft, Photon and Particle Interactions with Surfaces in Space, D. Reidel Publ. Co., Dordrecht-Holland, pp. 221-230.

14. Chang, K. W., and Bienkowski, G. K. (1970) Effects of electron emission on electrostatic probes at arbitrary pressures, Phys. of Fluids, 13:902-920.

15. DeForest, S. W. (1972) Spacecraft charging at synchronous orbit, J. Geophys. Res. 77:651-659.

16. Grard, R. J. L., Knott, K., and Pedersen, A. (1973) The influence of photoelectron and secondary electron emission on electric field measurements in the magnetosphere and solar wind, Photon and Particle Interaction with Surfaces in Space, D. Reidel Publ. Co., Dordrecht-Holland, pp. 163-189.

17. Akhiezer, A. I., and Akhiezer, I. A. (1975) Plasma Electrodynamics Volume 1: Linear Theory, Pergamon Press, Inc., New York.

18. Hamming, R. W. (1973) Numerical Methods for Scientists and Engineers, McGraw-Hill, New York pp. 505-515.

19. Langdon, A. B. (1970) Effects of the spatial grid in simulation plasmas, J. of Comp. Phys. 6:247-267.

20. Denavit, J. (1974) Discrete particle effects in whistler simulation, J. of Comp. Phys. 15:449-475.

Appendix A

In this appendix the method used to simulate a Maxwellian photosheath is briefly discussed. The computation time is much shorter if the speed and direction of the emitted particles are determined rather than the individual velocity components. The probability, p, that the speed, U, is less than or equal U_o is given by

$$p\,(U \leq U_o) = \sqrt{\frac{2}{\pi}} \int_0^{U_o} U^2\, e^{-U^2/2}\, dU \quad . \tag{A1}$$

where U and U_o are normalized to the thermal velocity, $\sqrt{kT/m}$.

One of us (GKY) has inverted Eq. A1 to give U_o as a function of p over the domain $0 \leq p \leq 1$. This domain was divided into six intervals and six empirical approximations determined. For $p \to 1^-$, the approach of Hastings[1] has been adopted.

The semiconvergent series for p as $p \to 1^-$ is

$$p = 1 - e^{-U_o^2/2}\, U_o \sqrt{\frac{2}{\pi}} \left(1 + \frac{1}{U_o^2} - \frac{1}{U_o^4} + \frac{3}{U_o^6} - \frac{15}{U_o^8} + \ldots\right) \tag{A2}$$

or

$$U_o^2 = -2 \ln (1 - P) + \ln (U_o^2) + \ln \frac{2}{\pi} + \ln \left(1 + \frac{1}{U_o^2} \ldots .\right)$$

substituting the lead term in the second term and ignoring terms of order U_o^{-2}

$$U_o \sim \sqrt{-2 \ln (1-p) + \ln [-2 \ln (1-p)] + \ln \frac{2}{\pi}} \tag{A3}$$

we have used

$$t = \sqrt{-2 \ln (1 - p) + a_1 + a_2 \ln [-2 \ln (1 - p)]} \tag{A4}$$

and

$$U_o = t + \frac{a_3 + a_4 p + a_5 p^2 + a_6 p^3}{1 + a_7 p + a_8 p^2 + a_9 p^2} \quad . \tag{A5}$$

For $p \to 0^+$, the form can be derived formally

$$p = \sqrt{\frac{2}{\pi}} \left[\frac{U_o^3}{3} - \frac{U_o^5}{10} + \frac{U_o^7}{56} \ldots \right] \quad . \tag{A6}$$

Let

$$U_o = S + C_3 S^3 + C_5 S^5 \quad . \tag{A7}$$

Substituting Eq. (A7) in Eq. (A6) gives

$$p = \sqrt{\frac{2}{\pi}} \left[\frac{S^2}{3} + (C_3 - \frac{1}{10}) S^5 + (C_5 + C_3^2 - \frac{C_3}{2} + \frac{1}{56}) S^7 + \ldots \right] .$$

The second and subsequent coefficients can be set to zero by appropriate choice of the C_n (that is, $C_3 = 0.1$, $C_5 = 0.0221428571$, etc.)

$$\text{Thus } p = \sqrt{\frac{2}{\pi}} \frac{S^3}{3} \qquad \text{or} \qquad S = (4.5\pi)^{1/6} p^{1/3} \quad . \tag{A8}$$

For $p \to 0^+$, substitute Eq. (A8) in Eq. (A7). In some of the intermediate intervals of p, slightly modified analytic forms provided greater accuracy.

Experiments show that photoelectrons produced inside the material surface are emitted with a cosine distribution relative to the surface normal.[2] A second random number, q, generates the appropriate angle.

The numbers p and q are generated by the function, RANF, resident on the AFGL CDC 6600. This generates random numbers uniformly between 0 and 1, excluding the end points. This function is a multiplicative congruential generator. Our use of the random numbers is not affected by the limitations pointed out by Marsaglia.[3] The "seed" for RANF is the quasirandom bit string which is generated by the computer's real time clock.

References

1. Hastings, C. Jr. (1955) Approximations for Digital Computers, Princeton University, Princeton, N.J.

2. Fadley, C.S. (1973) Theoretical aspects of x-ray photoelectron spectroscopy, Electron Emission Spectroscopy, Dekeyser, W., Fiermans, L., Vanderkelen, G., and Vernik, I., D. Reidel Publishing Co., Dordrecht-Holland, pp. 151-224.

3. Marsiglia, G. (1968) Random numbers fall mainly in the plains, Proceedings of the National Academy of Sciences 61:25-28.